New Altimetric Estimates of Mode-1 M_2 Internal Tides in the Central North Pacific Ocean

ZHONGXIANG ZHAO

Applied Physics Laboratory, University of Washington, Seattle, Washington

MATTHEW H. ALFORD

Applied Physics Laboratory, and School of Oceanography, University of Washington, Seattle, Washington

(Manuscript received 26 September 2007, in final form 21 January 2009)

ABSTRACT

New estimates of mode-1 M_2 internal tide energy flux are computed from an extended Ocean Topography Experiment (TOPEX)/Poseidon (T/P) altimeter dataset that includes both the original and tandem tracks, improving spatial resolution over previous estimates from O(500 km) to O(250 km). Additionally, a new technique is developed that allows separate resolution of northward and southward components. Half-wavelength features previously seen in unseparated estimates are shown to be due to the superposition of northward and southward wave trains. The new technique and higher spatial resolution afford a new view of mode-1 M_2 internal tides in the central North Pacific Ocean. As with all altimetric estimates, only the coherent or phase-locked signals are detectable owing to the long repeat period of the tracks. Emanating from specific generation sites consistent with predictions from numerical models, internal tidal beams 1) are as narrow as 200 km and 2) propagate a longer distance than previously observed. Two northward internal tidal beams radiating from the Hawaiian Ridge, previously obscured by coarse resolution and the southward Aleutian beam, are now seen to propagate more than 3500 km across the North Pacific Ocean to reach the Alaskan shelf. The internal tidal beams are much better resolved than in previous studies, resulting in better agreement with moored flux estimates.

1. Introduction

About 1 TW (10^{12} W) of surface tidal energy is lost in the deep ocean at rough topography such as seamounts, ridges, and trenches (Egbert and Ray 2000, 2003). Most of the conversion from surface to internal tides occurs at a small number of conversion sites (Egbert and Ray 2000; Simmons et al. 2004a; Nash et al. 2006). A major fraction of the tidal energy is converted into low-mode internal tides (St. Laurent and Garrett 2002; Althaus et al. 2003; Carter et al. 2008) and is transported a long distance from the generation sites (Hendry 1977; Dushaw et al. 1995; Ray and Mitchum 1996). The fate of these radiated internal tides remains poorly understood; nonetheless, theoretically they may dissipate in the processes of encountering strongly sheared currents, propagating onto near-critical continental slopes, scattering on the rough seafloor, and cascading to small-scale waves through parametric subharmonic instability (e.g., St. Laurent and Garrett 2002; MacKinnon and Winters 2005; Kunze et al. 2006; Alford et al. 2007).

Together with the wind, internal tides provide a major energy source to drive the large-scale meridional overturning circulation (MOC), with potential implications for global climate change (Munk and Wunsch 1998; Wunsch and Ferrari 2004; St. Laurent and Simmons 2006). It has been suggested that not only the total magnitude but also the geographic distribution of ocean mixing is necessary to study the MOC variability and to improve global ocean circulation models (Samelson 1998; Garrett 2003; Simmons et al. 2004b). Thus, it is important to understand the processes of generation, propagation, and dissipation of internal tides on the global scale (Rudnick et al. 2003; Gregg et al. 2003; Garrett and Kunze 2007).

The global patterns of low-mode internal tides have been investigated using a collection of historical moorings

Corresponding author address: Zhongxiang Zhao, 1013 NE 40th St., Seattle, WA 98105.
E-mail: zzhao@apl.washington.edu

DOI: 10.1175/2009JPO3922.1

© 2009 American Meteorological Society

Unauthenticated | Downloaded 06/22/21 02:32 PM UTC

(Wunsch 1975; Chiswell 1994; Alford 2003; Alford and Zhao 2007a,b). The small sea surface height anomaly (~2 cm) caused by mode-1 M_2 internal tides is also detectable from altimetric satellites, as first shown by Ray and Mitchum (1996, 1997) and subsequently by other researchers (Kantha and Tierney 1997; Ray and Cartwright 2001; Dushaw 2002; Chiswell 2006; Tian et al. 2006). Altimetric detection techniques may represent a great improvement over moored measurements owing to the near-global coverage of the satellites.

However, altimetric measurements have several shortcomings in studying internal tides: 1) They can only detect temporally coherent signals, potentially resulting in underresolution of phase-variable signals resulting from propagation through mesoscale eddy fields (Rainville and Pinkel 2006; Chiswell 2006; Alford and Zhao 2007a). 2) Propagation direction can only be determined from fitting plane waves over several adjacent ground tracks. The associated spatial smoothing results in a low bias, as noted by Ray and Cartwright (2001, henceforth RC01) and Dushaw (2002). 3) The presence of multiple sources, such as the Aleutian Ridge and the Hawaiian Ridge, can lead to potentially confusing interference patterns that can mask the signatures of individual sources (Fig. 1).

This paper, henceforth referred to as ZA09, presents new altimetric maps of energy flux in the North Pacific that improve on previous efforts by addressing 2) and 3) above. Regarding 2), RC01's altimetric fluxes computed from plane-wave fits (Fig. 1a, black arrows; data courtesy of R. Ray) are substantially weaker than moored observations (open-head arrows). Since the moored estimates are extracted by harmonic analysis and hence contain only the coherent mode-1 M_2 constituent, temporal incoherence, 1) above is not responsible. Instead, we show here that the underestimation is due to the heavy spatial smoothing associated with the plane-wave fits in 3° (latitude) × 4° (longitude) regions (Fig. 1a, black boxes), as suggested originally by RC01. In this study we add data from the tandem Ocean Topography Experiment (TOPEX)/Poseidon (T/P) mission spanning September 2002–October 2005, which lies halfway between the original tracks, doubling spatial resolution (Fig. 1b, dashed lines and black boxes). The resulting increased fluxes (Fig. 1b, black arrows) are more in line with moored values (open-head arrows), supporting this interpretation. This is not surprising given the narrowness of the beams in the more highly resolved maps (Fig. 1b).

Regarding 3), evidence for standing waves has long been noted in altimetric records (Ray and Mitchum 1996, 1997; Dushaw 2002). Here we consider these in some detail and develop a simple method for separately resolving the northward and southward components in these regions. The separately resolved fields (Fig. 2), together with the higher spatial resolution, offer a new and clearer view of the propagation of internal tide energy in the region. For example, northward energy impinging on the Alaskan continental shelf can be traced back over 3500 km to individual generation regions at the Hawaiian Ridge, in good agreement with simple ray-tracing models (Rainville and Pinkel 2006).

The remainder of the paper is arranged as follows. Section 2 briefly introduces the extended T/P altimeter dataset. Techniques are given in section 3. In section 4, the new flux estimates are presented and compared with previous altimetric fluxes, moored fluxes, and numerical model results. A summary and discussion follow.

2. Data

The T/P along-track gridded sea surface height anomaly (SSHA) data (product 157) are provided by the NASA Jet Propulsion Laboratory Physical Oceanography Distributed Active Archive Center (JPL/PO.DAAC). This dataset contains cycles from 11 to 481, spanning from January 1993 to October 2005. Each cycle contains 254 tracks and represents a collection of data where the ground track of the T/P satellite repeats itself every 9.9156 days. The ascending tracks (odd numbered) are in the northeast direction. The descending tracks (even numbered) are in the southeast direction. From cycle 365 to 368 (August to September 2002), the T/P satellite moved from original tracks westward to tandem tracks, halfway between the original tracks. In this study, the tandem tracks are labeled with an ending "T." The original tracks contain cycles from 11 to 364, and the tandem tracks contain cycles from 369 to 481. The combination of these two datasets halves the intertrack distance, effectively doubling the spatial resolution (Fig. 1) (Chelton and Schlax 2003). The *Jason-1* SSHA data, sampled along the T/P original tracks since January 2002, are not used in this study.

SSHA is defined as the difference between the sea surface height and the mean sea surface. The mean sea surface represents the position of the ocean surface averaged over a long time period to remove annual, semiannual, seasonal, and spurious sea surface height signals (Benada 1997). The sea surface height has been processed by applying standard corrections for atmospheric effects, effects due to surface conditions, ocean barotropic tides, and other contributions (Berwin 2003a). Ocean barotropic tides are removed using the Goddard/Grenoble Ocean Tide model (GOT99.2; Ray 1999). The SSHA data along each track are then gridded into standard latitude and longitude locations, with time interval 1.08 s and spatial interval 6.2 km (Berwin 2003b). In this

Unauthenticated | Downloaded 06/22/21 02:32 PM UTC

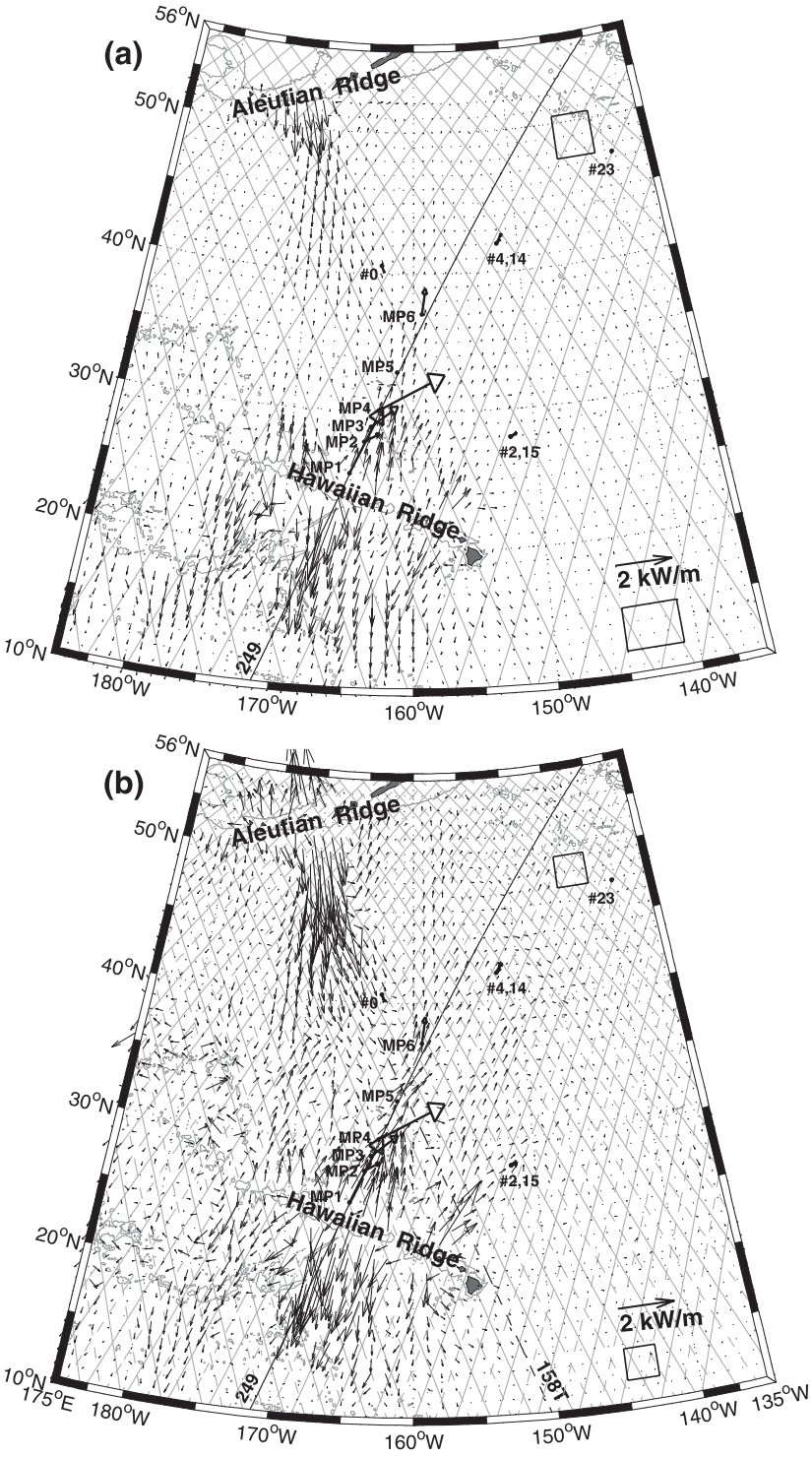

FIG. 1. Energy flux of mode-1 M_2 internal tides in the central North Pacific Ocean. Black arrows are altimetric fluxes obtained from (a) RC01 (kindly provided by R. Ray 2004, personal communication) and (b) this study. Open-head arrows show the coherent M_2 energy flux computed from moorings: 3000-m depth contours are plotted in gray; T/P tracks are plotted (gray), with tandem tracks used in this study plotted in dashed lines in (b); boxes indicate the size of plane-wave fits used in each study. Tracks 249 and 158T, highlighted in this study, are labeled.

Unauthenticated | Downloaded 06/22/21 02:32 PM UTC

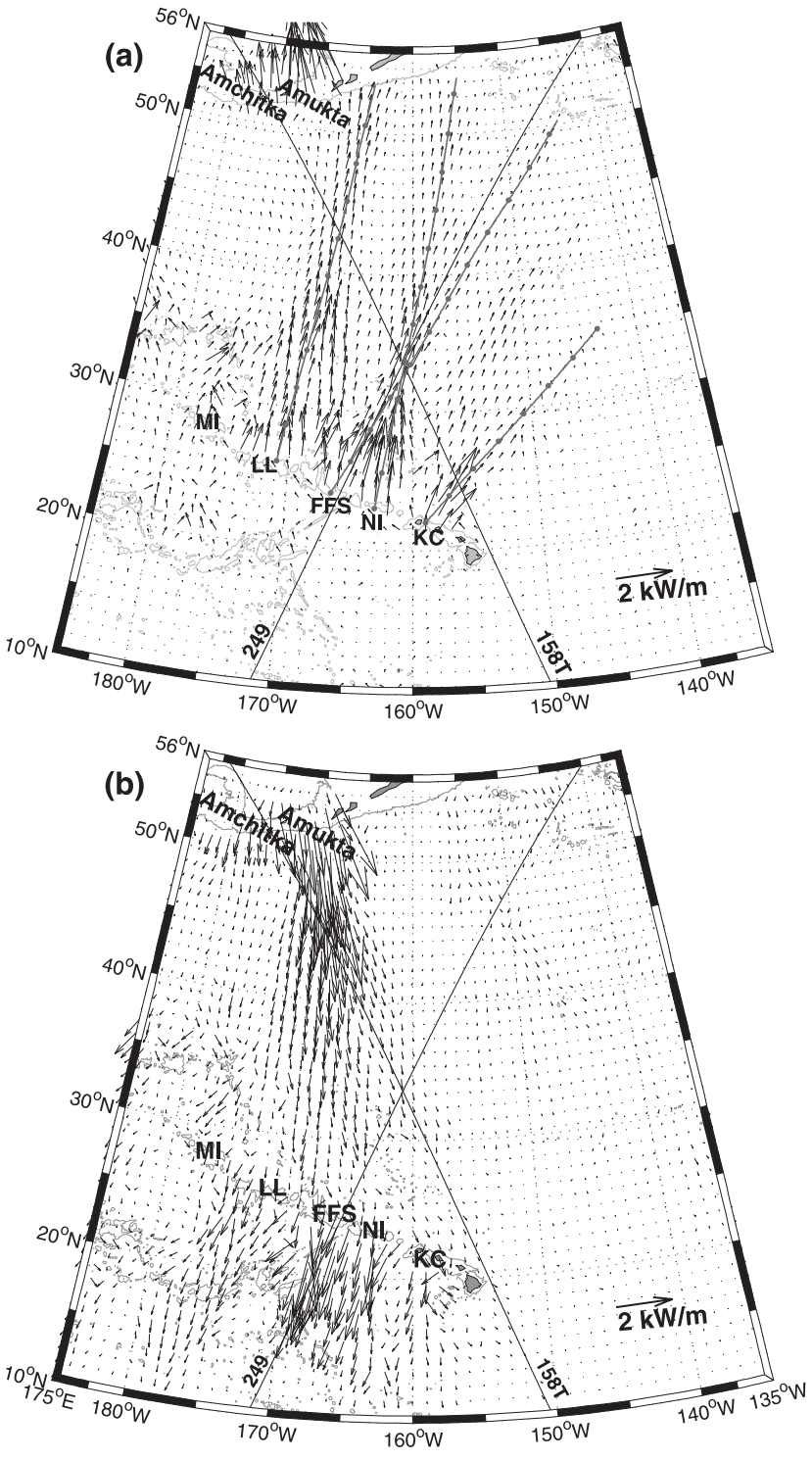

FIG. 2. As in Fig. 1, but for the separately resolved (a) northward and (b) southward components of energy flux. Five generation sites at the Hawaiian Ridge are labeled: the Kauai Channel (KC), Nihoa Island (NI), French Frigate Shoals (FFS), Laysan Island and Lisianski Island (LL), and Midway Island (MI), as well as two sites, Amchitka and Amukta, on the Aleutian Ridge. Four ray paths originating from the Hawaiian Ridge are computed for an eddy-free ocean (gray). Travel time is indicated in one-day increments with dots. Ray parameters are listed in Table 1.

Unauthenticated | Downloaded 06/22/21 02:32 PM UTC

study, measurements in waters shallower than 800 m are discarded. In addition, the along-track SSHA data are smoothed by a five-point running mean to reduce small-scale noise.

3. Methods

Raw and processed SSHA data along T/P tracks 249 and 158T are shown as examples (Figs. 3 and 4). The former is an ascending original track, and the latter is a descending tandem track (see Figs. 1 and 2 for location). The latitude limit 10°–52°N is selected to highlight the North Pacific Ocean.

a. Harmonic analysis

For continuity with previous work, we first extract the M_2 internal tides from the T/P altimeter data by harmonic analysis. Harmonic analysis is a standard method for extracting the constituents of predetermined frequencies from a time series of measurements (Emery and Thomson 2001, 392–404). The method has been widely used to extract the M_2 internal tides from T/P altimeter data (e.g., Ray and Mitchum 1996; Cummins et al. 2001; Tian et al. 2006). At every point along each T/P track, a time series of SSHA data is analyzed with a datum each T/P repeat period of 9.9156 days. Harmonic analysis uses a standard least squares method to determine the amplitude a and phase ϕ of each sinusoidal signal:

$$\eta(t) = a\cos(\omega_0 t - \phi), \tag{1}$$

where ω_0 is the M_2 tidal frequency. Previous altimetric analyses (e.g., Ray and Mitchum 1996; Ray and Cartwright 2001; Dushaw 2002) used high-pass spatial filtering with cutoff ~400 km to separate the barotropic and baroclinic tides; this is not necessary here since modeled barotropic tides have already been removed from the altimetric product used, as described above.

Raw SSHA data are dominated by non-M_2 motions, the vast majority of which are associated with the mesoscale eddy field. The raw SSHA along the T/P track 249 observed in all cycles has a peak-to-peak amplitude of ~40 cm (Fig. 3a). The harmonically extracted M_2 internal tide signal accounts for less than 5% of the raw signal (Fig. 3b).

Internal tide radiation northward and southward from the Hawaiian Ridge, consistent with signals first detected altimetrically by Ray and Mitchum (1996, 1997), is evident in decay of the amplitude (Fig. 3c, gray) and increase of the phase (Fig. 3d, gray) with distance northward and southward of the Hawaiian Ridge (24°N for this track, Fig. 3i). The along-track wavelength estimated from the along-track phase slope is about 160 km, consistent with the theoretical value (indicated with a horizontal bracket in Fig. 3c), calculated from climatological ocean stratification profiles (see the appendix).

In another example from the tandem track 158T (Figs. 4a–d), M_2 internal tides are seen radiating southward from the Aleutian Ridge, with wavelength about 160 km, as observed by Cummins et al. (2001). On this track, the amplitude does not decrease monotonically away from the Aleutian Ridge; rather, two peaks (indicated with gray shading in Fig. 4g) are seen near 32°–35° and 42°–45°N. As will be shown, these occur at the locations where the northward Hawaiian beams cross the southward Aleutian beam (Figs. 1 and 2). Particular attention is called to the half-wavelength amplitude modulations and nonmonotonic phase in Figs. 3 and 4, which are consistent with standing-wave patterns associated with these superposed wave trains, as hypothesized by previous investigators (RC01; Dushaw 2002). We consider these next.

b. Standing wave features

Consider the superposition of a northward and a southward mode-1 internal tide of unequal amplitude (Figs. 5a and 5b) and equal amplitude (Figs. 5c and 5d). In contrast to a propagating wave that has constant amplitude and constantly increasing phase (Figs. 5a and 5b, gray), the superposition of the unequal waves results in amplitude modulations of half the wavelength (Fig. 5a, black) and nonconstant phase increase (Fig. 5b, black). In the case of equal amplitudes (perfect standing wave), amplitude is zero twice per wavelength, and phase is piecewise constant, oscillating twice per wavelength between 0° and 180° (Figs. 5c and 5d, black).

As noted above, the half-wavelength oscillations observed in amplitude (Figs. 3c and 4c) and phase (Figs. 3d and 4d) are consistent with superposition of the northward and southward beams. They are particularly prominent at 32–35° and 42–45°N, just where the beams intersect (Fig. 4). These features motivate us to explore a method for resolving each wave train separately, presented in the next section.

c. Separation technique: Single tracks

A variation of harmonic analysis is used to separately resolve the northward and southward components contributing to the observed SSHA signals along each track. Instead of using data at a single location, data within one-half wavelength of each analysis location are input into a simple inverse model for traveling signals in each compass direction. The two solutions (one northward and one southward) that minimize the

Unauthenticated | Downloaded 06/22/21 02:32 PM UTC

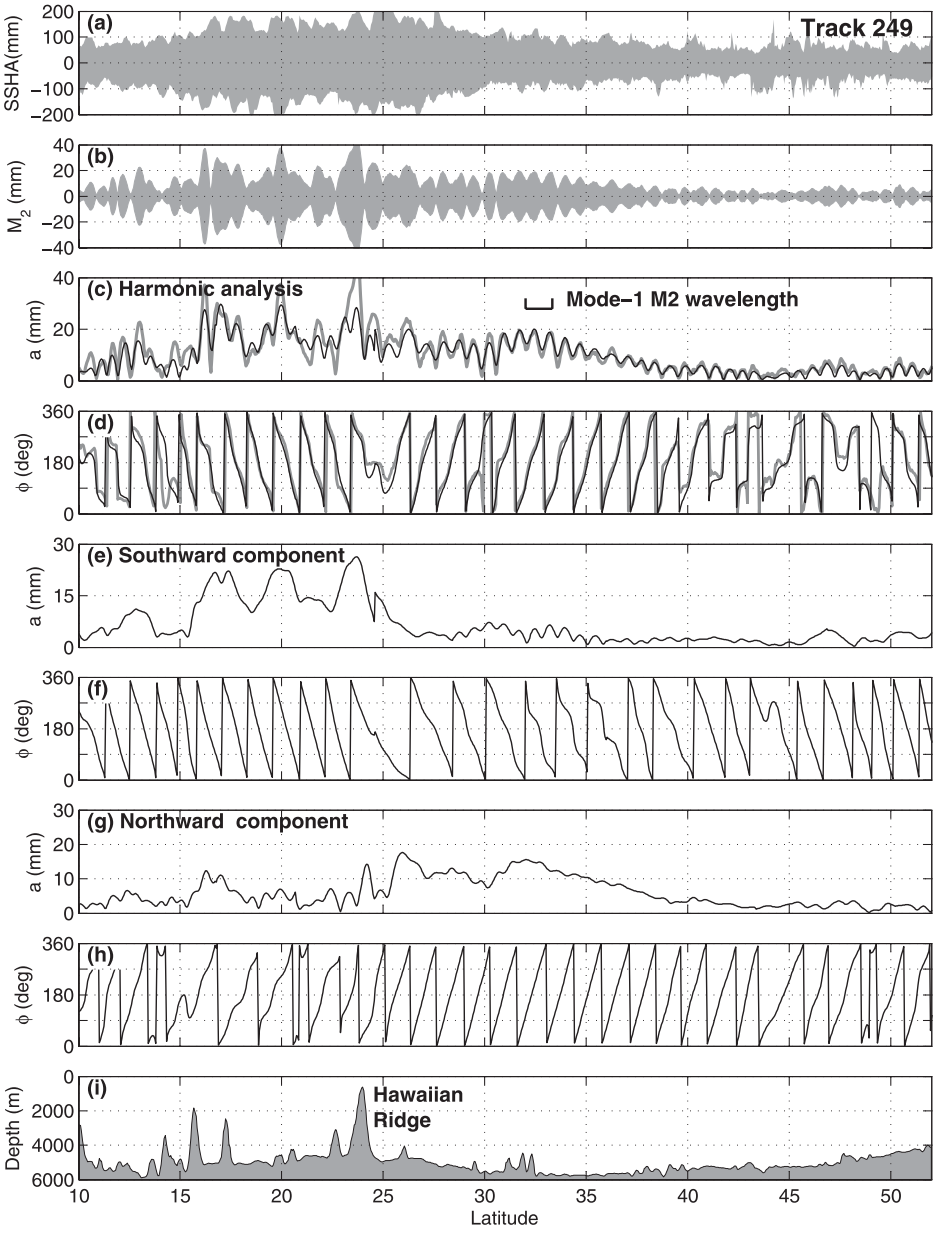

FIG. 3. Altimetric signals along T/P track 249: (a) raw sea surface height anomaly (SSHA) in all cycles; (b) the M_2 SSHA extracted by harmonic analysis; (c),(d) the M_2 amplitude and phase obtained by harmonic analysis (gray) and by superposing the southward and northward components (black); (e),(f) the M_2 amplitude and phase of the southward component; (g),(h) the M_2 amplitude and phase of the northward component. (i) Along-track bottom topographic profile. The theoretical along-track wavelength for a mode-1 M_2 internal tide (~160 km) is indicated in (c).

least squares residual variance are then retained. As will be shown, their superposition is nearly identical to that obtained from harmonic analysis. However, additional information is contained in the separated signals.

The model to be solved for is a mode-1 wave propagating in a direction θ relative to the T/P track:

$$\eta = a\cos(k_0 x\cos\theta - \omega_0 t - \phi), \tag{2}$$

where x is the along-track coordinate, t is time, ω_0 is the M_2 tidal frequency, and k_0 is the wavenumber of a mode-1 M_2 internal tide (determined from climatological ocean stratification profiles; see the appendix). At each along-track location, altimetry data SSHA(x, t) are

Unauthenticated | Downloaded 06/22/21 02:32 PM UTC

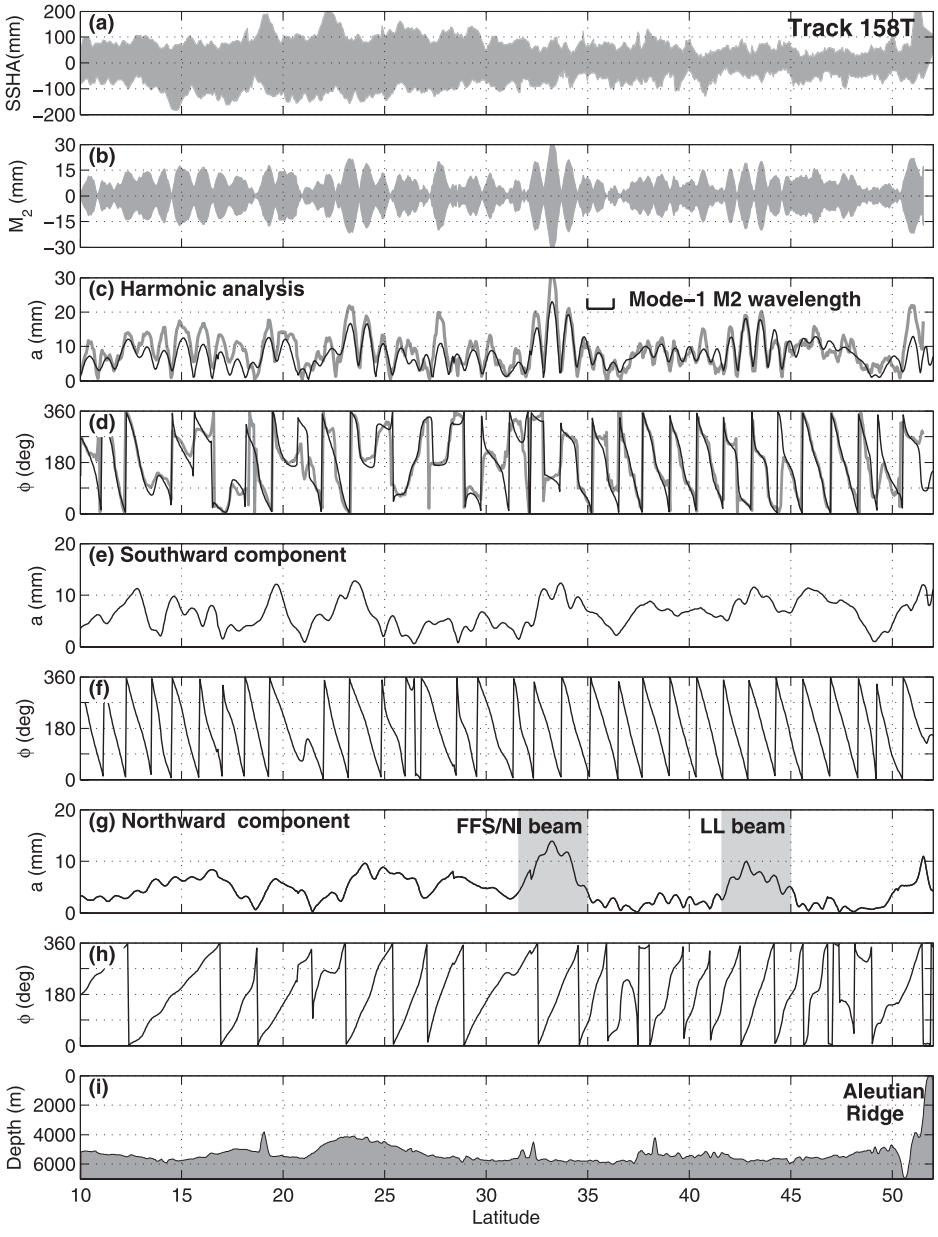

FIG. 4. As in Fig. 3, but for T/P track 158T. The locations of the northward FFS/NI and LL internal tidal beams are labeled in (g).

used to solve for amplitude a and phase ϕ for each direction θ. The northward and the southward solutions with the greatest amplitude, which also minimize the least squares error, are retained.

The method is demonstrated first in simple cases using synthetic data, then with real data, before presenting the results. Consider first a single mode-1 wave of amplitude 1 propagating toward $+x$ along an ascending track (indicated by the thick line in Fig. 6a). Model amplitude is plotted versus angle (with north at the top) and the track direction indicated. The method obtains the correct amplitude for $\theta = 0$, as expected. Evaluation of the model for other incident angles results in rapid attenuation of the solution owing to the mismatch between the actual and assumed wavelengths. Importantly, the sidelobes of the solution remain small, <0.1, for all values of θ more than $\sim 60°$ from the true direction. As a result, the amplitude and phase of superposed waves traveling in opposite directions along the track ($\theta = 0°$ and $180°$ in the case shown in Fig. 5) can be determined independently.

It remains to be shown that the method can extract superposed waves propagating obliquely relative to the

Unauthenticated | Downloaded 06/22/21 02:32 PM UTC

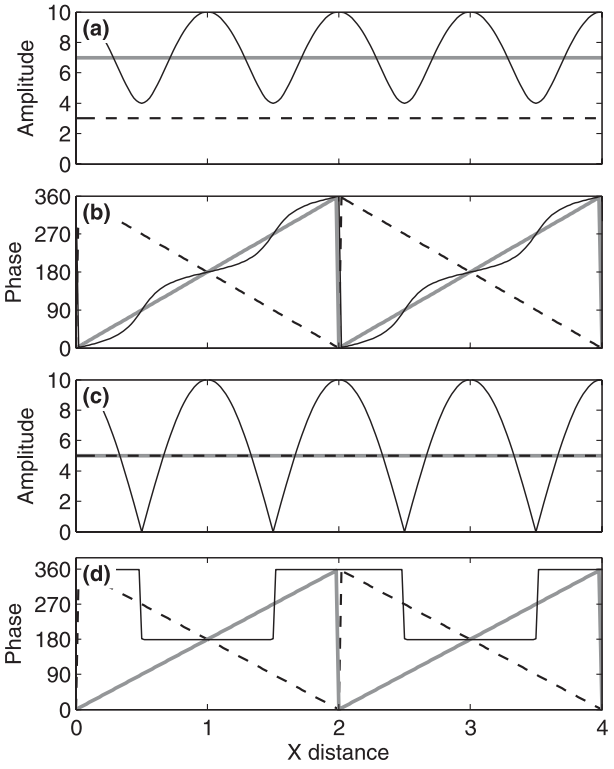

FIG. 5. (a) Amplitude and (b) phase of propagating waves in the positive (gray) and negative x directions (dashed). They have unequal amplitudes (7 and 3, respectively) so that their superposition is a partial standing wave (solid black). (c),(d) As in (a),(b) but for a full standing wave resulting from two waves of equal amplitude. Propagating waves have constant amplitude and linearly increasing phase, while the partial and full standing waves have half-wavelength oscillations in amplitude and phase. A full standing wave has a 180° phase jump at each node.

track in the presence of noise and other signals. We consider solutions from tracks 249 (Fig. 7a) and 158T (Fig. 7b) at their intersection point (33.5°N, 161°W). Past and present flux maps (Fig. 1) indicate the presence at this location of a strong northward signal toward ~60° (one Hawaiian beam) and a weaker southward signal toward ~280°(one Aleutian beam). As in the synthetic case, the model [Eq. (2)] is evaluated for each direction θ.

The angular response is symmetric with respect to each track since waves impinging from the left or right cannot be distinguished. Along track 249, a broad maximum around 60° is seen for waves propagating northward along the track, consistent with the strong fluxes from Hawaii, together with a weaker peak near 280°, consistent with the southward fluxes from the Aleutians. Measured peaks from track 158T coincide with these same directions. Their agreement with each other and with expected directions lends confidence in the method. Greater angular resolution is obtained in the plane-wave solutions, presented below, at the cost of spatial resolution.

The peaks at high incident angles in both tracks are associated with long along-track wavelengths via $\lambda_{\|} = \lambda_0/\cos\theta$. Though barotropic tides have been removed from our altimetry product, we conservatively reject signals $|\theta| > 60°$ (gray shading), consistent with along-track wavelengths longer than 320 km, to minimize contamination by the barotropic tide.

The model is then evaluated at each location along the track, and the northward and southward waves with the greatest amplitudes retained. Results are plotted for the range 10°–52°N for each track. As indicated above, the amplitude and phase from superposition of the two waves (panels c and d in Figs. 3 and 4, black lines) are in excellent agreement with the results from standard harmonic analysis (gray lines). Regions of disagreement likely represent interference between more than two wave trains and/or very obliquely propagating waves that are poorly resolved by our technique.

Considering the separated fields next (Figs. 3 and 4: panels e,f and g,h, respectively), strong signals such as the waves radiating northward (25°–40°N) and southward (15°–25°N) from the Hawaiian Ridge now appear in the appropriate panel. For both tracks, the southward (northward) components show much smoother amplitude, and monotonically increasing (decreasing) phase, than their harmonically analyzed counterparts (panels c,d), indicating that the components of the standing waves have been separated successfully. In addition, the standing wave regions identified previously are now seen as comparable amplitudes in their respective components. For example, northward amplitude peaks that appear in track 158T at 32°–35° and 42°–45°N (Fig. 4g) are associated with two northward internal tidal beams from the Hawaiian Ridge. Their along-track wavelength is noticeably longer than their southward components, consistent with their oblique angle of incidence. Their locations are consistent with sources at French Frigate Shoals and Nihoa Island (FFS/NI) and from Laysan Island and Lisianski Island (LL) (Fig. 2). Their along-track widths are about 320 km, implying real beam widths of ~200 km.

d. Plane-wave fitting and flux calculation

The along-track results are a useful partition of the gross northward and southward propagation and are of use for their higher spatial resolution, but multiple tracks are necessary to obtain more precise directional information—at the cost of spatial resolution. Our method closely follows that used by RC01, but we allow two waves of arbitrary direction rather than requiring

Unauthenticated | Downloaded 06/22/21 02:32 PM UTC

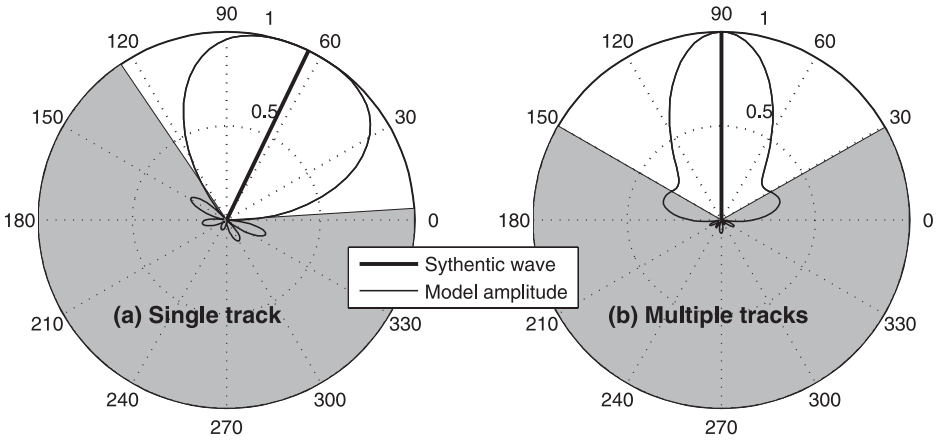

FIG. 6. (a) Model amplitude computed for each direction from data along a single track (see section 3c) for a synthetic wave of unit amplitude traveling along the track (heavy black). (b) Plane-wave model amplitude computed from multiple tracks for each direction (see section 3d) for a synthetic wave traveling toward the north (heavy black). In the gray regions, the model amplitude rapidly attenuates because of the mismatch between the actual and assumed directions.

them to be in opposite directions, as they did. Plane waves are fit in overlapping boxes of 250 km × 250 km, spanning three ascending tracks and three descending tracks (Fig. 8a).

As in the single-track calculation, a least squares model is solved for a wave propagating in a direction θ, now defined counterclockwise from true east:

$$\eta = a\cos(k_0 x\cos\theta + k_0 y\sin\theta - \omega_0 t - \phi), \qquad (3)$$

where x and y are now the east and north coordinates. As before, the model is evaluated for each direction θ. For a synthetic northbound wave, the angular resolution is substantially improved over the single-track calculation (Fig. 6b). The northbound wave and the southbound wave with the largest amplitudes are retained, as shown for a sample calculation from the same region considered above (Fig. 8b, arrows). Energy flux is then computed separately for each constituent as detailed in the appendix.

Amplitude peaks associated with waves propagating toward 60° and 280° are selected, consistent with the single-track results. They are the southward Aleutian and northward Hawaiian beams (see Fig. 2). Consistent with the rough angular resolution derived from the single-track results, we have chosen to reject waves

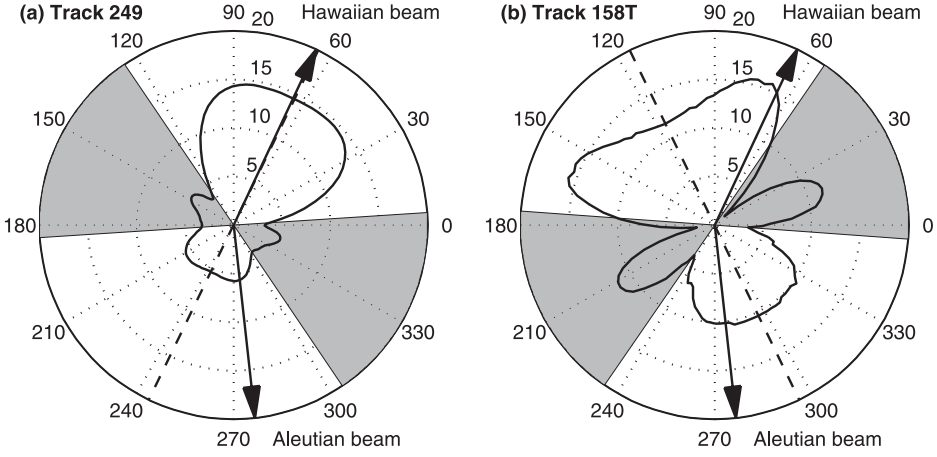

FIG. 7. Model amplitude versus direction for single-track calculation (see section 3c) at tracks (a) 249 and (b) 158T. The location is the intersection between the two tracks (33.5°N, 161°W). The dashed lines indicate the tracks 249 and 158T, respectively. The arrows show one Hawaiian beam and one Aleutian beam determined in plane-wave fitting (section 3d). Gray regions indicate angle ranges excluded from the calculation because of potential contamination by barotropic tidal signals.

Unauthenticated | Downloaded 06/22/21 02:32 PM UTC

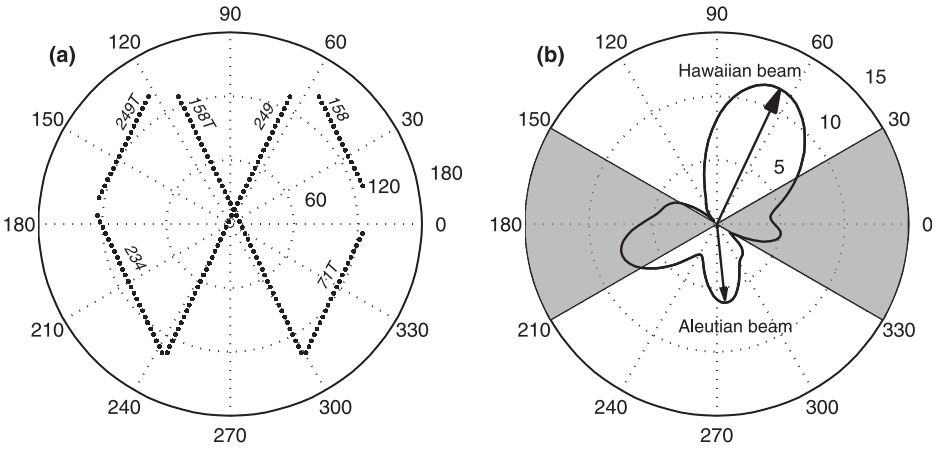

FIG. 8. (a) Ground tracks used in a sample 250 km × 250 km fitting region near 33.5°N, 161°W. (b) Amplitude versus wave direction. The arrows indicate the southward and northward waves chosen. Gray regions denote the angle ranges excluded from selection.

more than 60° from north–south (the mean alignment of the T/P tracks; Fig. 6b). Hence, the third wave propagating toward 200° is discarded, leading to a slight underestimation of the harmonic analysis amplitude (Fig. 4c).

4. Energy fluxes in the central North Pacific

a. Qualitative description

Following the plane-wave fitting method, the resulting maps of total energy flux (Fig. 1b) and the separated northward and southward components (Fig. 2) are presented next. We first describe the qualitative aspects of the new more highly resolved flux maps. An immediate observation is the increased magnitude of our total flux estimates (Fig. 1b) over those of RC01 (Fig. 1a), which, as noted, is attributed to increased spatial resolution. A quantitative comparison between the two altimetric estimates and moorings follows.

Northward flux is dominated by signals emanating from five generation regions at the Hawaiian Ridge, previously identified in models [areas 1–5 in Merrifield and Holloway (2002, henceforth MH02)]: the Kauai Channel (KC), Nihoa Island (NI), French Frigate Shoals (FFS), Laysan Island and Lisianski Island (LL), and Midway Island (MI). While these sources are all evident in the total flux (Fig. 1b), some quickly disappear into the broad southward beam emanating from the Aleutians.

By contrast, the northward Hawaiian beams are visible propagating great distances in the separated northward field (Fig. 2a). The FFS and NI beams, initially about 370 km apart, cross near 32°N about 950 km away from their sources (Fig. 2a). Fluxes from the LL, FFS, and NI beams are detectable as far north as the Alaskan continental shelf, over 3500 km from their sources. In particular, the northward fluxes visible in RC01's and our flux maps to the east of the Aleutian beam (48°–52°N, 164°–165°W) are now clearly identified with the LL and FFS sources. This increased detectability owes in part to the higher spatial resolution and partly because they were previously obscured by the Aleutian fluxes in maps of total flux. Their narrow width (~250–500 km) is still broader than the ~200 km implied in single-track data for the LL and FFS/NI beams (Fig. 4c and section 3c), indicating that they are likely still underresolved in the multitrack results, even with our improved spatial resolution.

To compare the locations of the beams with theoretical expectations, ray paths were computed assuming an eddy-free ocean using standard methods, described in Rainville and Pinkel (2006). Propagation speeds are computed from the *World Ocean Atlas 2005* annual-mean climatological ocean stratification data as described in the appendix. Calculations were initialized with generation sites and initial directions from MH02 (Table 1) and are overlaid in Fig. 2a. Successive daily locations, indicated with dots, give travel times (also shown in Table 1) from the source to the Alaskan shelf of ~10 days. The altimetrically detected flux agrees well with expected trajectories. (Since only the long-term coherent component is detected, no refraction by eddies would be measurable).

Southward internal tidal beams from the same five sources are seen in Fig. 2b, with the exception of MI (likely owing to signals too weak to be detected). The southward beams do not propagate as far as their northward counterparts (1000–1600 km). Two reasons

Unauthenticated | Downloaded 06/22/21 02:32 PM UTC

TABLE 1. Four northward internal tidal beams from the Hawaiian Ridge.

Source	Location (°N, °W)	Initial angle (°)	Distance (km)	Time (days)
KC	22, 159	49	2080	7
NI	23, 163	80	3500	11.4
FFS	24, 166.5	60	3500	11.4
LL	26, 171	82	3100	10

have been suggested to explain the more rapid attenuation. Johnston et al. (2003) suggest that the mode-1 internal tides are scattered into higher modes, and rendered undetectable, by the rough bottom topography of the Line Islands. Alternatively, Rainville and Pinkel (2006) suggest that the strong mesoscale eddies to the south of the Hawaiian Ridge cause the internal tides to lose phase coherence, also becoming undetectable to altimetric methods.

A broad southward beam emanates from conversion regions at the Amukta Pass (52°N, 172°W) and Amchitka Pass (52°N, 179°W), consistent with the previous observations (Cherniawsky et al. 2001; Cummins et al. 2001). (Strong northward fluxes from the Aleutian Ridge into the Bering Sea are also observed, but are not discussed further here.) The southward Amukta beam spreads out toward the south, as previously observed by RC01: 300 km wide at 50°N, it broadens to more than 1000 km wide at 40°N. One of its branches propagates across the North Pacific Ocean to reach the Hawaiian Ridge (Fig. 2b). As with the Hawaiian beams, the beam is detected farther than previously known, owing primarily to its masking by Hawaiian signals in previous maps of total flux.

b. Comparison with RC01 and moorings

As noted above, the new flux estimates exceed those of RC01 (Fig. 1a), which is attributed to improved spatial resolution. Since lateral resolution is not an issue for moorings, they are used as a benchmark for comparisons with each altimetric product. Subregions are selected centered on historical fixed-depth moorings (Fig. 9) and spanning a recent intensive experiment with six profiling moorings (Fig. 10). Ten moorings used in the comparisons are listed in Table 2.

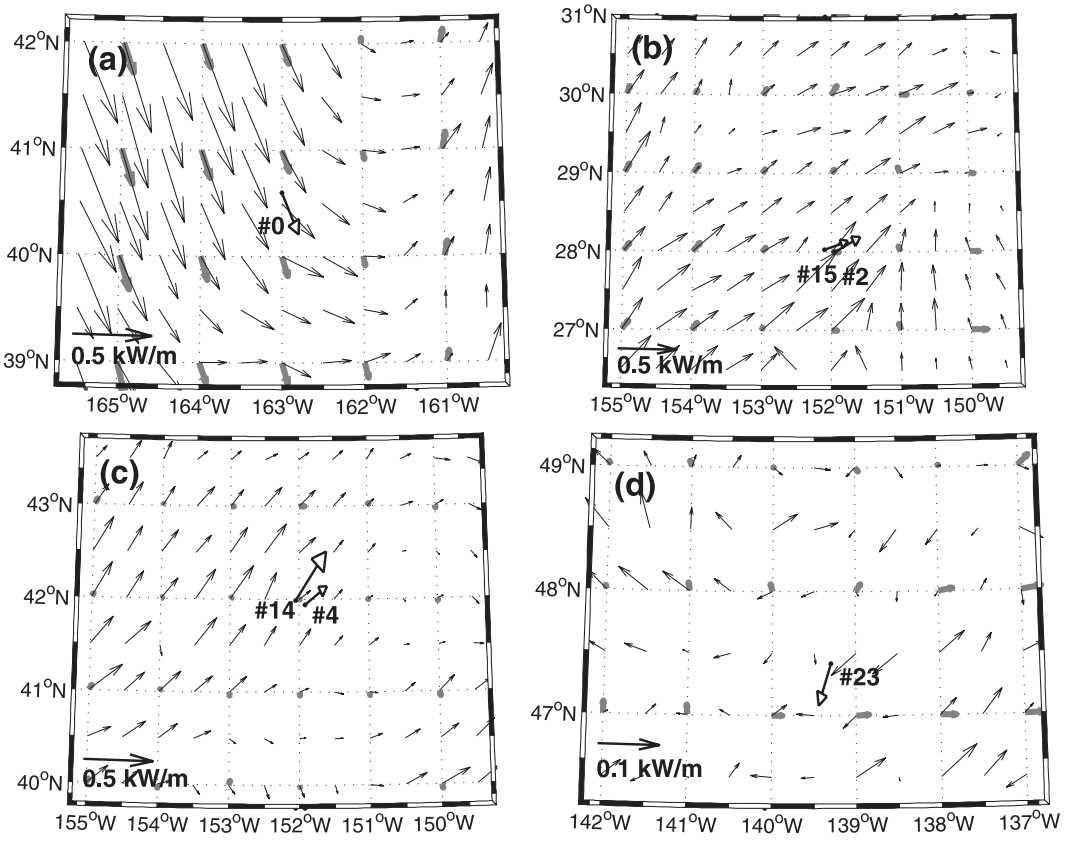

FIG. 9. Fluxes of the mode-1 M_2 internal tides from the new estimates in this study (ZA09, black), RC01 (gray), and historical moorings (open-head arrows). Information on the historical moorings can be found in Table 2.

Unauthenticated | Downloaded 06/22/21 02:32 PM UTC

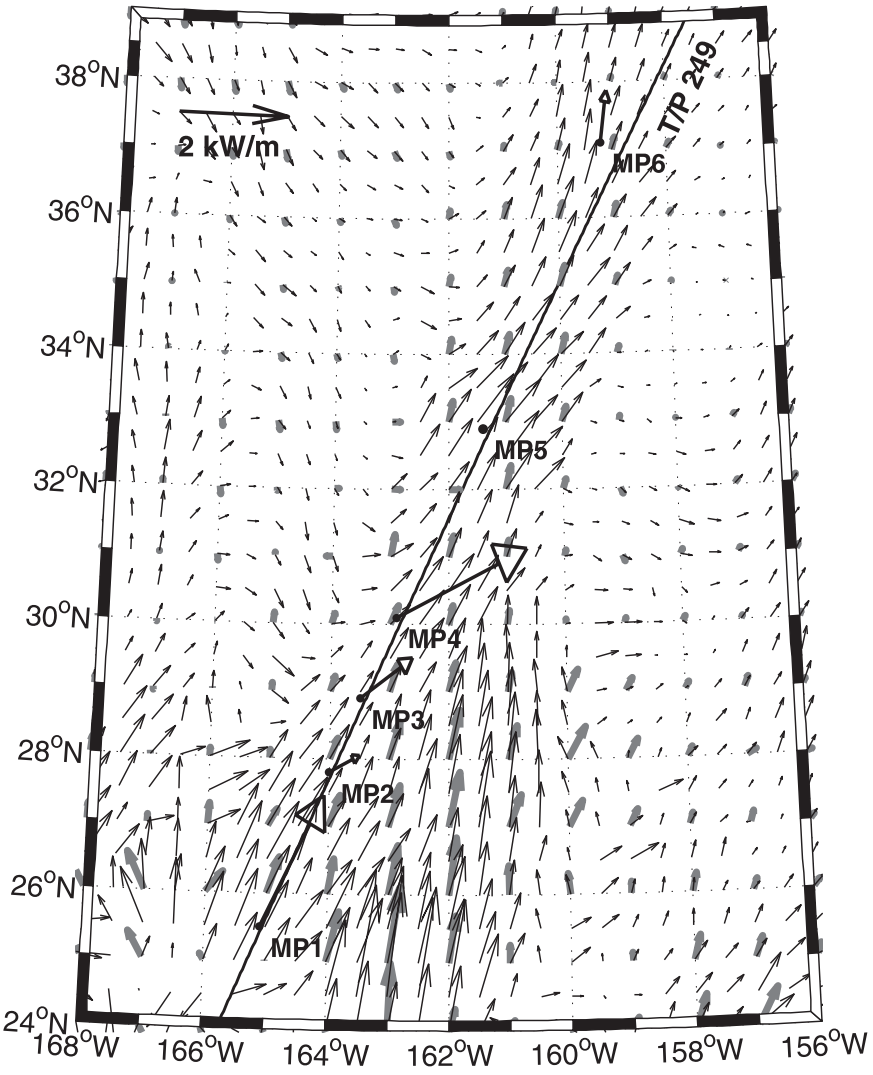

FIG. 10. Fluxes of mode-1 M_2 internal tides from the new estimates in this study (ZA09, black), RC01 (gray), and IWAP moorings (open-head arrows). Information on the IWAP moorings can be found in Table 2. The black line indicates T/P track 249.

Moored flux was computed via now-standard methods (Nash et al. 2005) from historical and the Internal Waves Across the Pacific (IWAP) moorings as described in detail in Alford and Zhao (2007a) and Alford et al. (2007), respectively. Briefly, velocity and isopycnal displacement from each measurement depth are projected into baroclinic vertical modes. Historical and IWAP moorings are sufficiently instrumented to resolve the first two and five baroclinic modes, respectively. The baroclinic pressure anomaly is then computed following Althaus et al. (2003). In both cases, flux is dominated by the mode-1 internal tide owing to the extreme redness of the pressure anomaly vertical wavenumber spectrum, as typically seen (Nash et al. 2005). The M_2 tidal constituent is then extracted by harmonic analysis. The uncertainty in the moored flux varies according to mooring geometry but is about 10%–20% (Nash et al. 2005).

In all subregions (Figs. 9 and 10) all three estimates (RC01, gray; ZA09, black; and moorings, open-head arrows) are generally in the same direction. (An exception is mooring MP4, which is larger and to the right of the altimetric and other moored estimates owing again to an interference pattern between the Aleutian and Hawaiian radiation, not resolved by the altimetric estimates, as described by Zhao et al. (2008, manuscript submitted to *J. Phys. Oceanogr.*, hereafter ZAMP). At mooring 23 (Fig. 9d), the RC01 fluxes are nearly zero, and the ZA09 fluxes are weak and without strong pattern. Hence, agreement with the mooring may be

Unauthenticated | Downloaded 06/22/21 02:32 PM UTC

TABLE 2. Moorings in the central North Pacific Ocean. For a historical mooring, the number of temperature/current instruments at the mooring is given; for an IWAP mooring, the depth range profiled is indicated (m). IWAP MP5 was excluded since its 4-day usable record was insufficient to separate the M_2 and S_2 constituents. Barotropic Electromagnetic and Pressure Experiment (BEMPEX).

Mooring	Expt	Year	Location (°N, °W)	Depth (m)	Duration (days)	Sampling (No./depths)	M_2 flux (kW m^{-1})
0	BEMPEX	1986	40.60, 163.00	5780	381	7	0.29
2	MiscPacific	1982	28.00, 151.95	5300	366	10	0.28
4	MiscPacific	1984	41.94, 151.92	5100	276	6	0.25
14	MiscPacific	1983	41.99, 152.05	5150	299	10	0.46
15	MiscPacific	1983	28.03, 152.10	5300	210	10	0.24
23	STORMS	1987	47.42, 139.30	4220	264	14	0.07
MP1	IWAP	2006	25.48, 165.15	4870	41	0–40, 85–1400, 3038	2.76
MP2	IWAP	2006	27.77, 163.97	5460	42	0–40, 85–1400, 3000	0.71
MP3	IWAP	2006	28.90, 163.49	5360	50	0–40, 85–1400, 3000	1.34
MP4	IWAP	2006	30.13, 162.88	5730	23	0–40, 85–1400, 3222	3.10
MP6	IWAP	2006	37.07, 159.22	5810	44	0–40, 85–1400, 2988	0.97

fortuitous. However, in general all three estimates are in the same direction, with the ZA09 fluxes closer to the moored values than those of RC01.

Because the flux determined from all methods is generally northeastward along T/P track 249 (Fig. 9), its magnitude versus range is next examined along this track for each method (Fig. 11). Flux does not decrease nonmonotonically, owing to a complicated interference pattern resulting from the various sources (Alford et al. 2007). In spite of this, it is clear that the total flux magnitude from ZA09 (black dashed) exceeds RC01 (gray) by about a factor of 2, but is still generally less than the flux estimated from moorings (dots) and MH02 (gray dashed).

Limited spatial resolution causes both altimetric estimates to underestimate the moored fluxes, as shown by several pieces of evidence. First, the ZA09 fluxes, when smoothed to 4° × 3° resolution, are in excellent agreement with RC01 (not shown).

A second piece of evidence comes from the fortuitous collinearity of the FFS beam with the T/P track 249, which enables calculation of fluxes from the single-track amplitudes by assuming fluxes are dominated by waves propagating northward along the track. The resulting estimate (black), which is not subject to finite resolution, exceeds the multitrack estimates south of 36°N. The along-track estimate is generally lower than the moored and modeled fluxes (Fig. 11) because it is also subject to temporal (beam drift) and spatial (along-track wave fitting) averaging. Figure 11 shows that the along-track and modeled results agree very well in their peak locations around 26°, 29°, and 32°N. This feature may be caused by 1) collinearity of the FFS beam with T/P track 249 and/or 2) interference of multiple beams (ZAMP; Rainville et al. 2009, manuscript submitted to *J. Phys. Oceanogr.*). Though one-to-one agreement is far from perfect, the general interference pattern indicated by the moored and modeled fluxes is replicated, suggesting that the beam is still too narrow at these locations (~200 km) to be resolved by the multitrack estimates.

Finally, multitrack and single-track flux estimates all agree north of 36°N and are in good agreement at 37°N with MP6. There, the widened beam is better resolved by the ZA09 multitrack estimate, suggesting that finite spatial resolution led to underestimation where the beam was narrower. This general improvement with range (owing to wider, hence better resolved, beams) is supported by the observation that our altimetric estimates are in better agreement with the historical moorings (Fig. 9) than with the IWAP moorings (Fig. 10).

5. Summary and discussion

New altimetric estimates of M_2 internal-tide energy flux in the North Pacific have been presented, improving over previous efforts in 1) spatial resolution and 2) separately resolved northward and southward components. Previously observed half-wavelength features in amplitude and phase are now clearly identified with standing wave patterns stemming from interference between northward and southward beams from Hawaii and the Aleutians, respectively. Beams are seen to be narrower than previously thought, and still marginally resolved even with our addition of tandem tracks. In spite of this, they are now clearly detectable, propagating across the Pacific basin.

This longevity has implications for the mixing done by internal tides. Since the still-inadequate spatial resolution and the insensitivity to higher modes and phase-variable signals cause these fluxes to be lower bounds on the true values, the detection of appreciable coherent mode-1 fluxes impinging on the basin edges is

Unauthenticated | Downloaded 06/22/21 02:32 PM UTC

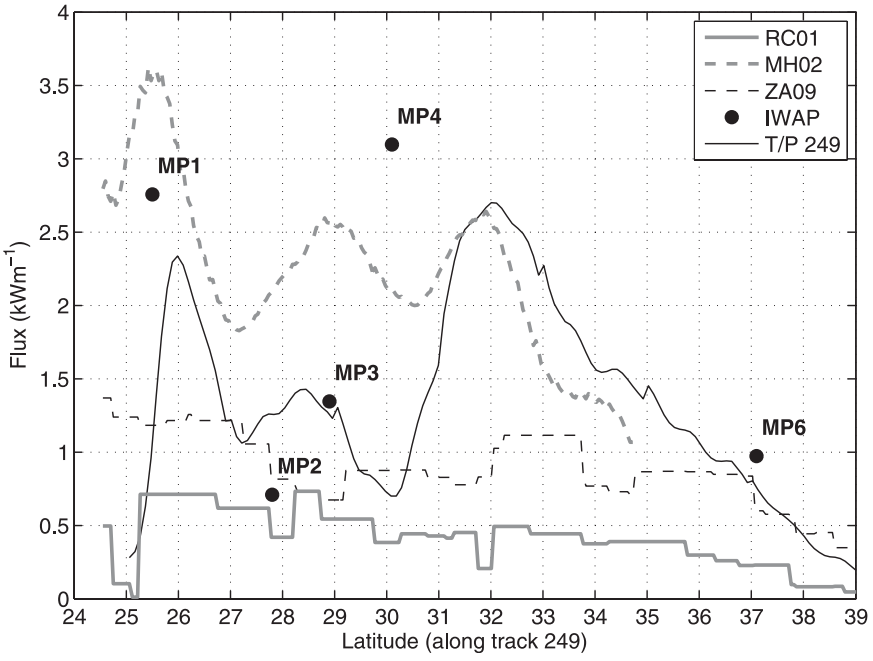

FIG. 11. Flux magnitude of mode-1 M_2 internal tide on T/P track 249 from RC01 (gray), MH02 (gray dashed), this study (ZA09, black dashed), moorings (dots), and from single-track estimates assuming northward propagation along TP249 (black; see text).

noteworthy. Owing to the need to carefully assess the effects of these attenuative factors, which is attempted in a parallel effort (M. H. Alford et al. 2008, unpublished manuscript), we feel it is premature to attempt to compute the divergence of the flux field. A careful census, beyond the scope of this work, of the ocean's internal tide sinks may feature breaking on near-critical slopes with more prominence than previously thought.

Time series from several other altimetric satellites, for example, *Jason-1*, *European Remote Sensing Satellites-1* and *-2* (*ERS-1/-2*), the *Environmental Satellite* (*Envisat*), and the *Geosat Follow-On* (*GFO*), are now long enough to extract M_2 internal tides. Ongoing work seeks to combine all of these, each with different repeat period and ground track, to obtain still more highly resolved estimates—ideally over the globe instead of the North Pacific alone. In addition, other constituents such as S_2 and K_1 should be evaluated. Much work remains.

Acknowledgments. This work was supported by NSF Grant OCE0424717. We thank R. Ray and D. Cartwright for providing their seminal altimetric estimates of internal tides, M. Merrifield and T. M. S. Johnston for providing their POM results, L. Rainville and R. Pinkel for providing their ray-tracing model, and B. Dushaw, M. Foreman, and J. Cherniawsky for their help in processing T/P altimeter data. We thank two reviewers for their insightful suggestions that greatly improved this paper.

APPENDIX

Energy Flux, Group, and Phase Speed Calculation

In an ocean of constant depth, an internal tide can be represented by a sum of discrete vertical normal modes that only depend on the buoyancy frequency profile $N(z)$ and the water depth H. The modal structure of vertical displacement is described by the eigenvalue equation:

$$\frac{d^2\Phi(z)}{dz^2} + \frac{N^2(z)}{C^2}\Phi(z) = 0, \tag{A1}$$

subject to boundary conditions $\Phi(0) = \Phi(-H) = 0$, where $\Phi(z)$ is the eigenfunction and C is the eigenspeed.

Supposing that the corresponding modal structure of pressure and horizontal velocity is described by $\Pi(z)$, the relations between $\Pi(z)$ and $\Phi(z)$ are (Gill 1982)

$$\Pi(z) = \rho_0 C_n^2 \frac{d\Phi(z)}{dz}, \tag{A2}$$

and

Unauthenticated | Downloaded 06/22/21 02:32 PM UTC

$$\Phi(z) = -\frac{1}{N^2\rho_0}\frac{d\Pi(z)}{dz}. \quad \text{(A3)}$$

For each mode, the internal tide obeys the dispersion relation:

$$\omega^2 = k_n^2 C_n^2 + f^2, \quad \text{(A4)}$$

where ω is the tidal frequency, f is the inertial frequency, and k_n the wavenumber. Thus, the phase speed is

$$C_p = \frac{\omega}{k_n} = \frac{\omega}{(\omega^2 - f^2)^{1/2}} C_n, \quad \text{(A5)}$$

and the wavenumber is

$$k_n = \frac{(\omega^2 - f^2)^{1/2}}{C_n}. \quad \text{(A6)}$$

The pressure $p(z)$, horizontal velocity $u(z)$ and $v(z)$, and vertical displacement $\xi(z)$ for the mode-1 M_2 internal tide can be written in terms of sea surface tide amplitude a, and mode-1 vertical modal structures $\Pi_1(z)$ and $\Phi_1(z)$ as (Chiswell 2006)

$$p(z) = a\rho_0 g\Pi_1(z), \quad \text{(A7)}$$

$$u(z) = a\frac{g\omega k_1}{\omega^2 - f^2}\Pi_1(z), \quad \text{(A8)}$$

$$v(z) = -a\frac{igfk_1}{\omega^2 - f^2}\Pi_1(z), \quad \text{(A9)}$$

and

$$\xi(z) = -a\rho_0 g\Phi_1(z). \quad \text{(A10)}$$

The vertically integrated energy flux of the mode-1 internal tide can be calculated by

$$\begin{aligned} F &= \frac{1}{2}\int_{-H}^{0} u(z)p(z)dz \\ &= \frac{1}{2}a^2\left[\frac{\rho_0 g^2\omega k_1}{\omega^2 - f^2}\int_{-H}^{0}\Pi_1^2(z)dz\right] \\ &= \frac{1}{2}a^2 F_n, \end{aligned} \quad \text{(A11)}$$

where F_n is the term in the brackets, meaning the flux of the M_2 internal tide with 1-cm amplitude at the surface. Note that the energy flux is proportional to the amplitude squared.

Ocean stratification data are from the *World Ocean Atlas 2005* (Antonov et al. 2006; Locarnini et al. 2006), and topography data are from Smith and Sandwell (1997). As an example, Fig. A1 shows the phase speed, wavenumber, F_n, and depth along 150°W.

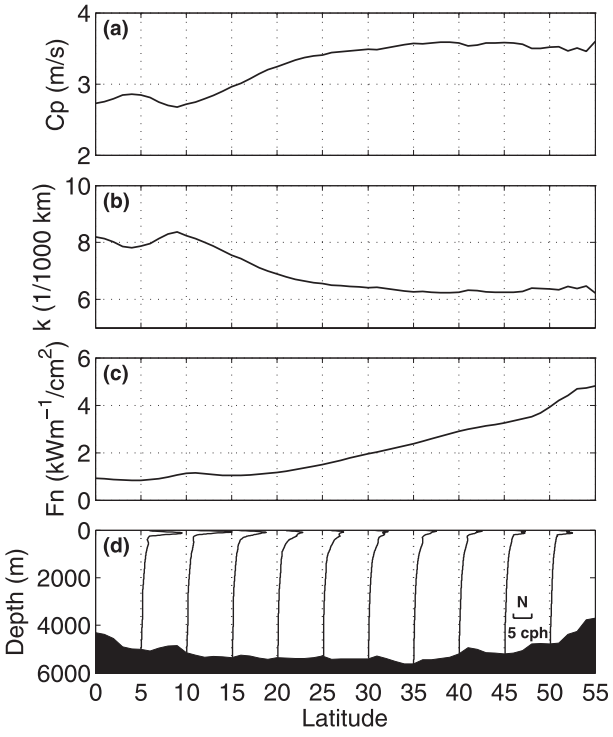

FIG. A1. Parameters of mode-1 M_2 internal tides along 150°W: (a) phase speed, (b) wavenumber, (c) flux of M_2 internal tide with 1-cm sea surface height anomaly [as F_n defined in Eq. (A11)], and (d) bottom topographic profile and buoyancy frequency profiles (N: cph).

REFERENCES

Alford, M. H., 2003: Redistribution of energy available for ocean mixing by long-range propagation of internal waves. *Nature,* **423,** 159–162.

——, and Z. Zhao, 2007a: Global patterns of low-mode internal-wave propagation. Part I: Energy and energy flux. *J. Phys. Oceanogr.,* **37,** 1829–1848.

——, and ——, 2007b: Global patterns of low-mode internal-wave propagation. Part II: Group velocity. *J. Phys. Oceanogr.,* **37,** 1849–1858.

——, J. A. MacKinnon, Z. Zhao, R. Pinkel, J. Klymak, and T. Peacock, 2007: Internal waves across the Pacific. *Geophys. Res. Lett.,* **34,** L24601, doi:10.1029/2007GL031566.

Althaus, A. M., E. Kunze, and T. B. Sanford, 2003: Internal tide radiation from Mendocino Escarpment. *J. Phys. Oceanogr.,* **33,** 1510–1527.

Antonov, J. I., R. A. Locarnini, T. P. Boyer, A. V. Mishonov, and H. E. Garcia, 2006: *Salinity*. Vol. 2, *World Ocean Atlas 2005,* NOAA Atlas NESDIS 61, 182 pp.

Benada, J. R., 1997: PO.DAAC Merged GDR (TOPEX/POSEIDON) Generation B user's handbook. Version 2.0, JPL D-11007, Physical Oceanography DAAC, NASA JPL, 185 pp.

Unauthenticated | Downloaded 06/22/21 02:32 PM UTC

Berwin, R., 2003a: Along-track gridded sea surface height anomaly for TOPEX/Poseidon and Jason-1—User's reference manual. Physical Oceanography DAAC, NASA JPL, 9 pp.

——, 2003b: TOPEX/Poseidon sea surface height anomaly product—User's reference manual. Physical Oceanography DAAC, NASA JPL, 15 pp.

Carter, G. S., and Coauthors, 2008: Energetics of M_2 barotropic-to-baroclinic tidal conversion at the Hawaiian Islands. *J. Phys. Oceanogr.,* **38,** 2205–2223.

Chelton, D. B., and M. G. Schlax, 2003: The accuracies of smoothed sea surface height fields constructed from tandem satellite altimeter datasets. *J. Atmos. Oceanic Technol.,* **20,** 1276–1302.

Cherniawsky, J. Y., M. G. G. Foreman, W. R. Crawford, and R. F. Henry, 2001: Ocean tides from TOPEX/Poseidon sea level data. *J. Atmos. Oceanic Technol.,* **18,** 649–664.

Chiswell, S. M., 1994: Vertical structure of the baroclinic tides in the central North Pacific subtropical gyre. *J. Phys. Oceanogr.,* **24,** 2032–2039.

——, 2006: Altimeter and current meter observations of internal tides: Do they agree? *J. Phys. Oceanogr.,* **36,** 1860–1872.

Cummins, P. F., J. Y. Cherniawsky, and M. G. G. Foreman, 2001: North Pacific internal tides from the Aleutian Ridge: Altimeter observations and modeling. *J. Mar. Res.,* **59,** 167–191.

Dushaw, B. D., 2002: Mapping low-mode internal tides near Hawaii using TOPEX/POSEIDON altimeter data. *Geophys. Res. Lett.,* **29,** 1250, doi:10.1029/2001GL013944.

——, B. D. Cornuelle, P. F. Worcester, B. M. Howe, and D. S. Luther, 1995: Barotropic and baroclinic tides in the central North Pacific Ocean determined from long-range reciprocal acoustic transmissions. *J. Phys. Oceanogr.,* **25,** 631–647.

Egbert, G. D., and R. D. Ray, 2000: Significant dissipation of tidal energy in the deep ocean inferred from satellite altimeter data. *Nature,* **405,** 775–778.

——, and ——, 2003: Semi-diurnal and diurnal tidal dissipation from TOPEX/Poseidon altimetry. *Geophys. Res. Lett.,* **30,** 1907, doi:10.1029/2003GL017676.

Emery, W. J., and R. E. Thomson, 2001: *Data Analysis Methods in Physical Oceanography*. 2nd rev. ed., Elsevier, 638 pp.

Garrett, C., 2003: Internal tides and ocean mixing. *Science,* **301,** 1858–1859.

——, and E. Kunze, 2007: Internal tide generation in the deep ocean. *Annu. Rev. Fluid Mech.,* **39,** 57–87.

Gill, A. E., 1982: *Atmosphere–Ocean Dynamics*. Academic Press, 662 pp.

Gregg, M. C., T. B. Sanford, and D. P. Winkel, 2003: Reduced mixing from the breaking of internal waves in equatorial waters. *Nature,* **422,** 513–515.

Hendry, R. M., 1977: Observations of the semidiurnal internal tide in the western North Atlantic Ocean. *Philos. Trans. Roy. Soc. London,* **286A,** 1–24.

Johnston, T. M. S., M. A. Merrifield, and P. E. Holloway, 2003: Internal tide scattering at the Line Islands Ridge. *J. Geophys. Res.,* **108,** 3365, doi:10.1029/2003JC001844.

Kantha, L. H., and C. C. Tierney, 1997: Global baroclinic tides. *Prog. Oceanogr.,* **40,** 163–178.

Kunze, E., E. Firing, J. M. Hummon, T. K. Chereskin, and A. M. Thurnherr, 2006: Global abyssal mixing inferred from lowered ADCP shear and CTD strain profiles. *J. Phys. Oceanogr.,* **36,** 1553–1576.

Locarnini, R. A., A. V. Mishonov, J. I. Antonov, T. P. Boyer, and H. E. Garcia, 2006: *Temperature*. Vol. 1, *World Ocean Atlas 2005,* NOAA Atlas NESDIS 61, 182 pp.

MacKinnon, J. A., and K. B. Winters, 2005: Subtropical catastrophe: Significant loss of low-mode tidal energy at 28.9°. *Geophys. Res. Lett.,* **32,** L15605, doi:10.1029/2005GL023376.

Merrifield, M. A., and P. E. Holloway, 2002: Model estimates of M_2 internal tide energetics at the Hawaiian Ridge. *J. Geophys. Res.,* **107,** 3179, doi:10.1029/2001JC000996.

Munk, W., and C. Wunsch, 1998: Abyssal recipes II: Energetics of tidal and wind mixing. *Deep-Sea Res. I,* **45,** 1977–2010.

Nash, J. D., M. H. Alford, and E. Kunze, 2005: Estimating internal wave energy fluxes in the ocean. *J. Atmos. Oceanic Technol.,* **22,** 1551–1570.

——, E. Kunze, C. M. Lee, and T. B. Sanford, 2006: Structure of the baroclinic tide generated at Kaena Ridge, Hawaii. *J. Phys. Oceanogr.,* **36,** 1123–1135.

Rainville, L., and R. Pinkel, 2006: Propagation of low-mode internal waves through the ocean. *J. Phys. Oceanogr.,* **36,** 1220–1236.

Ray, R. D., 1999: A global ocean tide model from TOPEX/Poseidon altimetry: GOT99.2. NASA Tech. Memo. 1999-209478. Goddard Space Flight Center, Greenbelt, MD, 58 pp.

——, and G. T. Mitchum, 1996: Surface manifestation of internal tides generated near Hawaii. *Geophys. Res. Lett.,* **23,** 2101–2104.

——, and ——, 1997: Surface manifestation of internal tides in the deep ocean: Observations from altimetry and island gauges. *Prog. Oceanogr.,* **40,** 135–162.

——, and D. E. Cartwright, 2001: Estimates of internal tide energy fluxes from Topex/Poseidon altimetry: Central North Pacific. *Geophys. Res. Lett.,* **28,** 1259–1262.

Rudnick, D. L., and Coauthors, 2003: From tides to mixing along the Hawaiian Ridge. *Science,* **301,** 355–357.

Samelson, R. M., 1998: Large-scale circulation with locally enhanced vertical mixing. *J. Phys. Oceanogr.,* **28,** 712–726.

Simmons, H. L., R. W. Hallberg, and B. K. Arbic, 2004a: Internal wave generation in a global baroclinic tide model. *Deep-Sea Res. II,* **51,** 3043–3068.

——, S. R. Jayne, L. C. St. Laurent, and A. J. Weaver, 2004b: Tidally driven mixing in a numerical model of the ocean general circulation. *Ocean Modell.,* **6,** 245–263.

Smith, W. H. F., and D. T. Sandwell, 1997: Global sea floor topography from satellite altimetry and ship depth soundings. *Science,* **277,** 1956–1962.

St. Laurent, L., and C. Garrett, 2002: The role of internal tides in mixing the deep ocean. *J. Phys. Oceanogr.,* **32,** 2882–2899.

——, and H. L. Simmons, 2006: Estimates of power consumed by mixing in the ocean interior. *J. Climate,* **19,** 4877–4890.

Tian, J., L. Zhou, and X. Zhang, 2006: Latitudinal distribution of mixing rate caused by the M_2 internal tide. *J. Phys. Oceanogr.,* **36,** 35–42.

Wunsch, C., 1975: Internal tides in the ocean. *Rev. Geophys. Space Phys.,* **13,** 167–182.

——, and R. Ferrari, 2004: Vertical mixing, energy, and the general circulation of the oceans. *Annu. Rev. Fluid Mech.,* **36,** 281–314.

Unauthenticated | Downloaded 06/22/21 02:32 PM UTC